

Diagnostics of Eccentricities and Bar/End-Ring Connector Breakages in Polyphase Induction Motors through a Combination of Time-Series Data Mining and Time-Stepping Coupled FE-State Space Techniques

John F. Bangura¹, Richard J. Povinelli², Nabeel A.O. Demerdash², Ronald H. Brown²

¹Black & Decker

701 East Joppa Road, TW100
Towson, MD 21286

²Department of Electrical and Computer Engineering

Marquette University, 1515 W. Wisconsin Ave.
Milwaukee, WI 53233

Abstract – This paper develops the foundations of a technique for detection and categorization of dynamic/static eccentricities and bar/end-ring connector breakages in squirrel-cage induction motors that is not based on the traditional Fourier transform frequency domain spectral analysis concepts. Hence, this approach can distinguish between the “fault signatures” of each of the following faults: eccentricities, broken bars, and broken end-ring connectors in such induction motors. Furthermore, the techniques presented here can extensively and economically predict and characterize faults from the induction machine adjustable speed drive design data without the need to have had actual fault data from field experience. This is done through the development of dual-track studies of fault simulations and hence simulated fault signature data. These studies are performed using our proven Time Stepping Coupled Finite Element-State Space method to generate fault case performance data, which contain phase current waveforms and time-domain torque profiles. Then from this data, the fault cases are classified by their inherent characteristics, so called “signatures” or “fingerprints”. These fault signatures are extracted or “mined” here from the fault case data using our novel Time Series Data Mining technique. The dual-track of generating fault data and mining fault signatures was tested here on dynamic and static eccentricities of 10% and 30% percent of airgap height as well as cases of 1, 3, 6, and 9 broken bars and 3, 6, and 9 broken end-ring connectors. These cases were studied for proof-of-principle in a 208-volt, 60-Hz, 4-pole, 1.2-hp, squirrel cage 3-phase induction motor. The paper presents faulty and healthy performance characteristics and their corresponding so-called phase space diagnoses that show distinct fault signatures of each of the above mentioned motor faults.

I. INTRODUCTION

Three-phase induction motors are presently in common use in a majority of electronically controlled ac adjustable/variable speed drives. During the past twenty years, there have been continuing efforts at studying and diagnosing of induction motor faults and associated performance characteristics as outlined in a major bibliographic paper by Benbouzid [1]. As stated in [1] “performing reliable and accurate fault detection and diagnosis requires understanding the cause and effect of motor faults to motor performances.” The bulk of the motor fault diagnostics papers cited in reference [1], such as references [2-6], rely substantially on frequency domain Fourier transform spectral analysis of motor currents. This paper does not rely on such frequency domain spectral analysis concepts, which do not distinguish very well the specific fault types. This is not the case here in identifying the

fault types. The accrued advantages of our new techniques will become apparent to the reader in the results presented in this paper. Accordingly, this paper demonstrates a method for not only simulating fault conditions but also more specific identification of faults in induction machine adjustable speed drives (IMASDs).

Our approach to the problem of diagnosing faults in IMASDs is new and unique. First, knowing the design details of a motor-drive system, we can generate data for a plethora of fault conditions by Time Stepping Coupled Finite Element-State Space (TSCFE-SS) [2, 7-10] simulations. This is without the need to encounter and acquire data for such faults in actual field experience with IMASDs. Second, using Time Series Data Mining (TSDM) [11, 12], hidden patterns and nuances of differences between healthy performance signatures and various fault signatures can be identified. These fault signatures reveal the severity (percentage of airgap height) of dynamic and static eccentricities, the severity (approximate number) of broken squirrel-cage bars, and the severity (approximate number) of broken end-ring connectors. That is, this approach automatically and efficiently identifies and makes use of the data of these fault signatures in fault diagnostics.

The faulty operations being studied here include: 10% and 30% degrees of static and dynamic eccentricities, as well as 1, 3, 6, and 9 broken bars in addition to 3, 6, and 9 broken end-ring connectors [2, 9]. The advantage of this dual track method lies in its rigor in predicting effects of motor faults on performance. The second portion of this dual track identifies and extracts hidden patterns and nuances that are characteristic and predictive of specific faults through data mining of the fault signatures.

Accordingly, this paper presents the development of a comprehensive set of algorithms for fault simulation, and fault identification/diagnosis in IMASDs. Specifically, we deal here with motor shaft eccentricities and one broken bar in a side-by-side comparison with other squirrel cage breakages (broken bars and broken connectors). Initial broken bar and broken connector analysis was given in an earlier paper [13], and only an update of these results is given here for the purposes of comprehensive comparison between eccentricities and squirrel-cage breakages.

II. TIME STEPPING COUPLED FINITE ELEMENT-STATE SPACE METHOD

The TSCFE-SS technique computes on a time instant-by-instant basis (time profiles/waveforms) the input phase and line currents, voltages, developed power, and torque of a motor as functions of the particular magnetic circuit, winding layouts, and materials as well as inverter (power conditioner) operating conditions. Computations include the full effects of interaction of machine space harmonics with time-domain harmonics due to modern fast electronic switching on overall motor-controller/drive performance [10, 14]. Thus, the TSCFE-SS algorithms can also be used in parametric design studies.

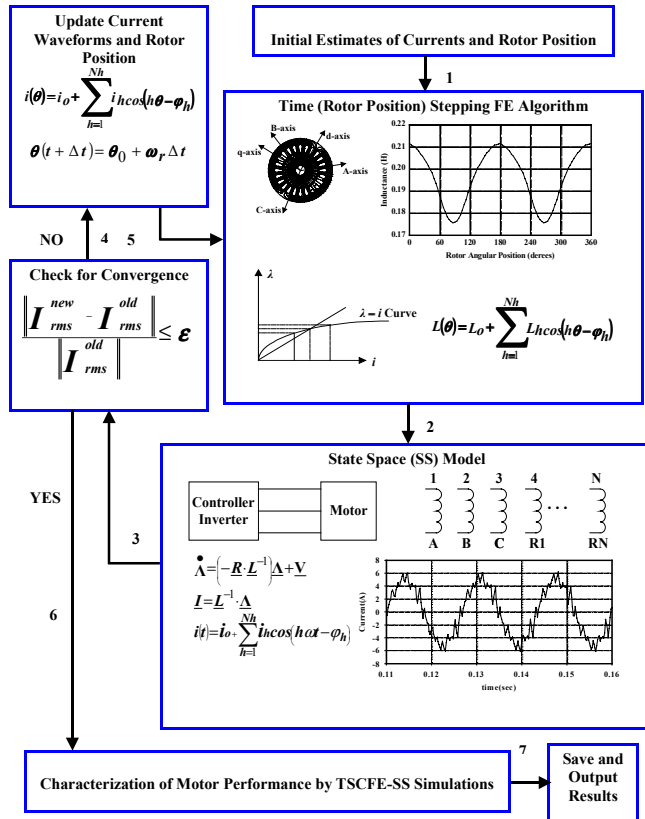


Fig. 1. Functional Block-Diagram/Flow Chart of the TSCFE-SS Method.

The TSCFE-SS aspect fully incorporates the nonlinear effects of magnetic saturation in the machine and makes full use of the natural machine winding's frame of reference, for details see [2, 7-10]. Also, see Fig. 1 for the functional flow chart block diagram, which summarizes the essence of this approach. Hence, again this assures inclusion of all significant space harmonics due to the physical design and nonlinear nature of the motor's magnetic circuit, as well as the time harmonics generated from the inverter switching in the motor-drive modeling and simulations. Accordingly, the simulated fault signatures are derived from time-domain phase current and voltage waveforms, and from simulated

instantaneous torque profiles that rigorously incorporate the motors' design characteristics.

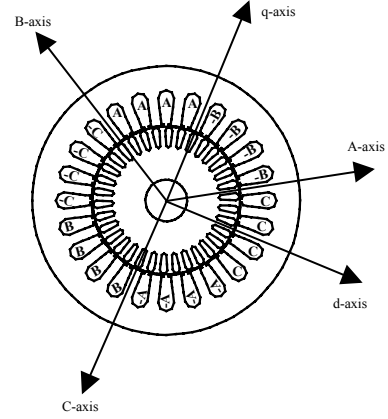


Fig. 2. Motor Cross Section

The state model for the 1.2 hp motor, the cross-section of which is given in Fig. 2, was derived from generalized machine theory using the natural abc frame of reference, and the inverter and machine models were integrated. The overall machine-inverter network model of Fig. 3 ensued. The state variables in this model are the a, b, and c armature windings' flux linkages as well as the 34 flux linkages of the 34 squirrel-cage loops under healthy motor conditions, see the motor's cross section of Fig. 2 and the developed squirrel-cage loop diagram of Fig. 4. Again, for details, references [2, 7-10] should be consulted. To represent bar breakages and end-ring connector breakages the squirrel-cage loops need to be disturbed according to patterns such as shown in Figs. 5 and 6, respectively. For further details reference [2] should be consulted.

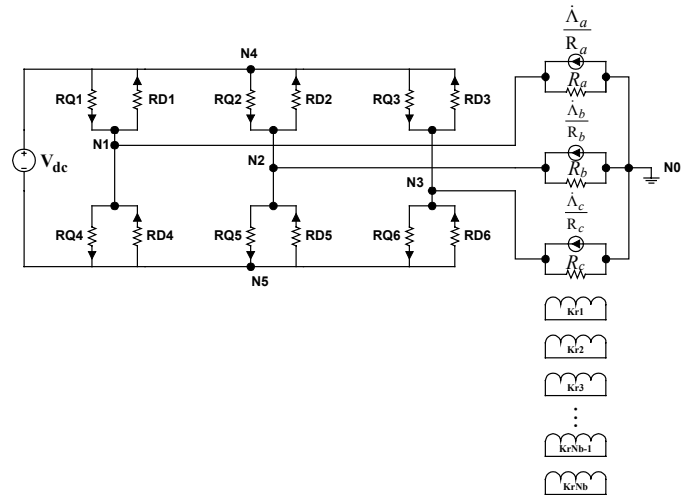


Fig. 3. Schematic of Inverter-Motor Network Graph With Y-Connected Stator Winding Configuration

As to the cases of static and dynamic eccentricities, those were modeled by disturbing the rotor's location and consequently its FE grid's location as shown schematically in

Fig. 7. The schematic in Fig. 7 can represent the static and dynamic eccentricities depending on which of the two points separated by the distance, δ , are made to be the axis of rotor rotation, for details reference [9] should be consulted further. In essence, in static eccentricity the airgap takes the shape of a stationary crescent-like pattern, while in dynamic eccentricity the airgap take the shape of a continuously modulated revolving crescent.

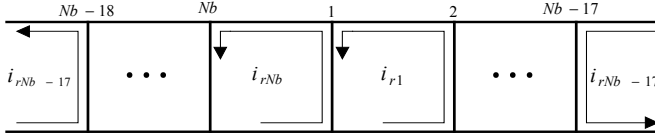


Fig. 4. Schematic Representation of the Modeling of a Healthy Cage

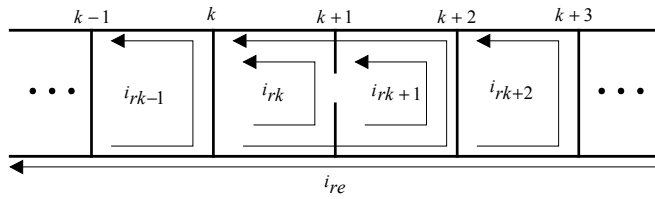


Fig. 5. Schematic Representation of the Modeling of a Broken Rotor Bar

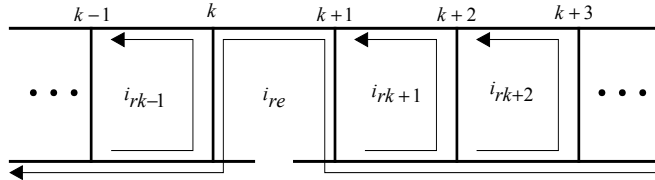


Fig. 6. Schematic Representation of the Modeling of a Broken End-Ring Connector

The TSCFE-SS model yields the steady state time-domain profiles of the change in all winding (loop) inductances under actual time-varying saturation conditions, and all the steady state time-domain profiles/waveforms of the developed machine torque and all the 37 winding currents (3 are the a, b, and c stator armature currents, the remainder are the squirrel-cage loop currents whose number is 34 or less depending on the pattern of bar/connector breakages being simulated).

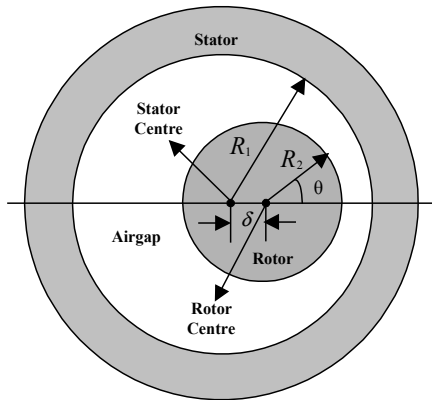


Fig. 7. Schematic Representation of Airgap Eccentricity

III. TIME SERIES DATA MINING METHOD

The TSDM method, the second track of the dual track approach, overcomes limitations (including stationarity and linearity requirements) of traditional time series analysis techniques by adapting data mining concepts for analyzing time series. Based soundly in dynamical systems theory [15], the TSDM method reveals hidden patterns in time series data (current and voltage waveforms as well as time-domain torque profiles). A clear distinction is shown here between the various faulty and healthy modes of motor operation. Our approach provides a definite new advantage over frequency-spectrum Fourier transform techniques particularly used for fault diagnostics by earlier investigators [2-6].

A process called time-delay embedding [16] is used to transform the torque time series into a reconstructed state space, also called a phase-space. Given the first difference torque time series $\Delta T = \{\Delta \tau(k), k = 2, \dots, N\}$, where $\Delta \tau = \tau(k) - \tau(k-1)$, k is a time index, and N is the number of observations, a two dimensional phase-space is created by plotting $\Delta \tau(k-10)$ on the x-y plane's abscissa and $\Delta \tau(k)$ on the ordinate. See Figs. 14 through 25 for examples of such phase-spaces.

The feature used for distinguishing between reconstructed phase-spaces generated for different healthy and faulty modes of motor operation is the so-called radius of gyration [17] (which is used in this work as a fault identification parameter) around the center of mass of the points in the phase-space, where each point in the phase-space is given a unit mass. The radius of gyration, r , is calculated as follows [17]:

$$r = \sqrt{\frac{\sum_{k=1+l}^N d(k)^2}{N-l}}, \quad (1)$$

where the distance, $d(k)$, between the center of mass and the k^{th} point in the phase-space, is:

$$d(k)^2 = (x(k) - \mu_0)^2 + (x(k-l) - \mu_l)^2, \quad (2)$$

and μ_0 and μ_l , the centers of mass for their respective dimensions, are:

$$\mu_m = \frac{\sum_{k=1+l}^{N-l+m} x(k)}{N-l}. \quad (3)$$

Additionally, l is the time lag of the phase space, N is the number of observations, and $x(k)$ is the time series observation at time index k , see reference [16] for details of time-delay embedding process. It should be pointed out that $d(k)$ is the distance of the k^{th} phase-space "point" from the center of mass of the phase-space "points". Since we are using a two dimensional phase-space, which is formed by

plotting $x(k-l)$ on the x-y plane's abscissa and $x(k)$ on the ordinate, the square of the distance is calculated by summing the squares of the differences between the phase-space point's value in each dimension and its corresponding center of mass for that same dimension. The value μ_m is the center of mass for each phase-space dimension.

This radius of gyration feature is a sufficient first approximation of the phase-space to allow distinguishing between the motor's healthy mode of operation and various squirrel-cage breakage faults being presented here. It is also sufficient to identify the degree of the eccentricity, e.g. it allows the differentiation between modes of operation of 10% and 30% degrees of eccentricities. However, we introduce here a second feature, which is required to differentiate between the dynamic and static eccentricities of the same degree. This second feature is the standard deviation, σ , of the radius of gyration, which is defined as follows:

$$\sigma = \sqrt{\frac{(N-l) \sum_{k=1+l}^N (d(k)^2)^2 - \left(\sum_{k=1+l}^N d(k)^2 \right)^2}{(N-l)(N-l-1)}} \quad (4)$$

Given a motor's time-domain torque first difference as a time series (profile), and its corresponding reconstructed phase-space, the algorithm, for determining the unknown operating mode of the motor from which the time-domain torque profile was sampled, is best described as follows:

Algorithm IDENTIFYMODE (R, r, Σ, σ)

Input. A set $R = \{r_1, r_2, \dots, r_n\}$ of the radii of gyration of the known operating modes, where n is the number of known operating modes. The radius of gyration for the unknown mode, r . A set $\Sigma = \{\sigma_1, \sigma_2, \dots, \sigma_m\}$ of the standard deviations of the radii of gyration for the eccentricity modes of operation, where m is the number of known eccentricity modes of operation. The standard deviation of the radius of gyration for the unknown mode, σ .

Output. The identified mode of operation.

1. $i = \text{index}(\min\{|r' - r| : r' \in R\})$. The index operator yields the "index of the mode" with the closest radius of gyration to the unknown mode.
2. **if** i is an index for an eccentricity mode of operation
3. **then** Form Σ' a subset of Σ with the standard deviations of the radii of gyration that have the same degree of eccentricity as the mode of operation corresponding to the index, i . For example if the index i corresponds to a 30% dynamic eccentricity, Σ' has as elements the standard deviations of the radii of gyration for the 30% static eccentricity and the 30% dynamic eccentricity.
4. $j = \text{index}(\min\{|\sigma' - \sigma| : \sigma' \in \Sigma'\})$. The index operator yields the "index of the mode" with the closest standard deviation of the radius of gyration to the standard deviation of the radius of gyration of the unknown mode.
5. **return** the eccentricity mode of operation corresponding to the index j .
6. **else return** the mode of operation corresponding to the index i .

IV. TSCFE-SS SIMULATIONS

Simulations of the healthy cage case; the 10% and 30% static and dynamic eccentricity cases; as well as the 1, 3, 6, and 9 broken bar cases; the 3, 6; and 9 broken end-ring connector cases were generated using our TSCFE-SS method. The resulting torque profiles for the simulation of the healthy rotor/cage case; the 10% and 30% static and dynamic eccentricity cases; and 1 broken bar case are given in Figs. 8 through 13, respectively. The torque profile simulations for the other cases were presented in [13]. The reconstructed phase-spaces of the torque first difference time series corresponding to the torque profile simulations for the healthy rotor/cage case and all the faulty rotor/cage cases mentioned above are illustrated in Figs. 14 through 25, respectively.

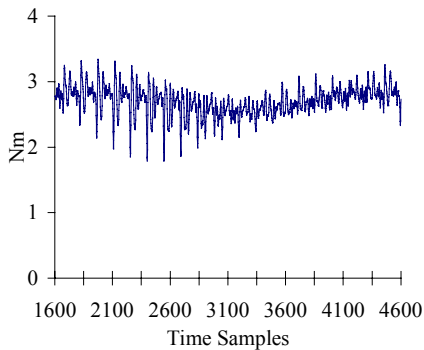


Fig. 8. Healthy Motor Torque Profile

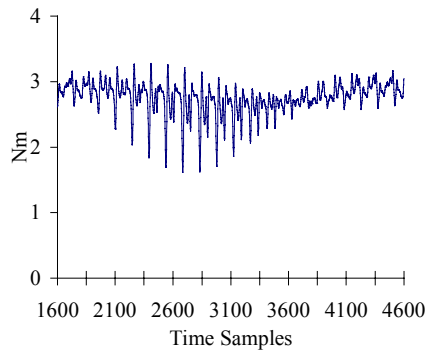


Fig. 9. 10% Static Eccentricity Torque

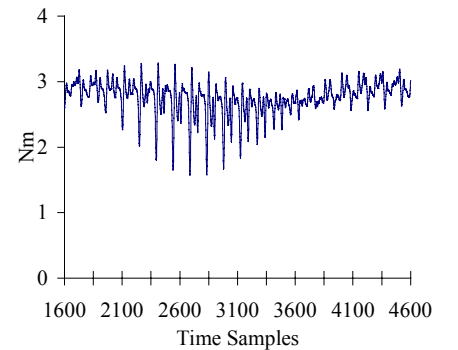


Fig. 10. 30% Static Eccentricity Torque

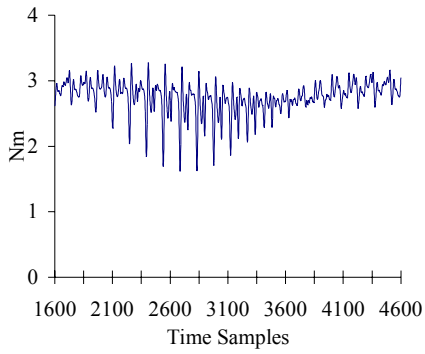


Fig. 11. 10% Dynamic Eccentricity Torque

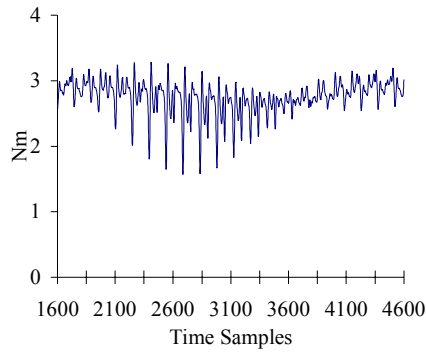


Fig. 12. 30% Dynamic Eccentricity Torque

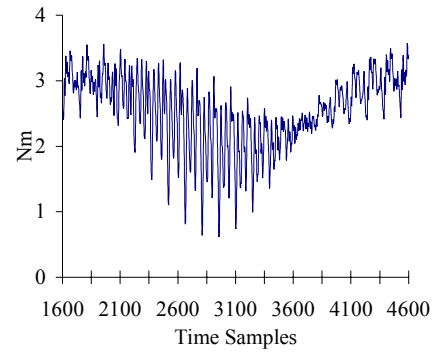


Fig. 13. One Broken Bar Torque Profile

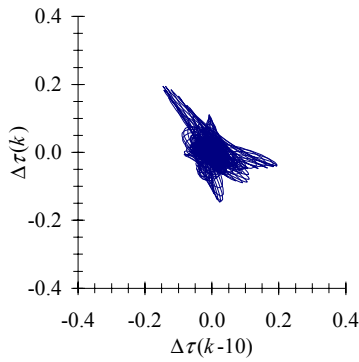


Fig. 14. Healthy Motor Torque First Difference Phase-Space

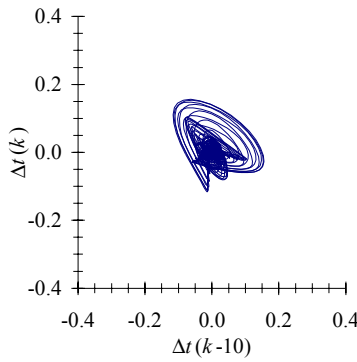


Fig. 15. 10% Static Eccentricity Torque First Difference Phase-Space

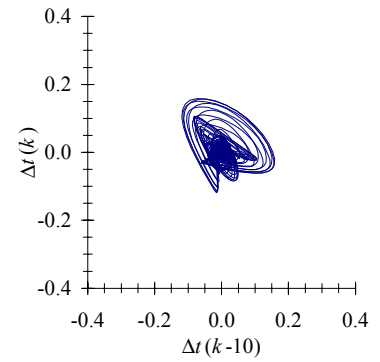


Fig. 16. 30% Static Eccentricity Torque First Difference Phase-Space

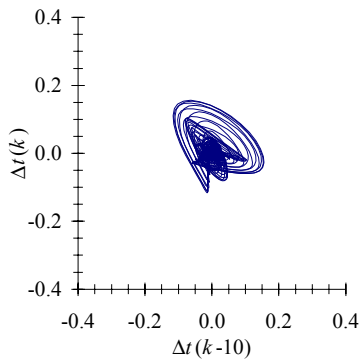


Fig. 17. 10% Dynamic Eccentricity Torque First Difference Phase-Space

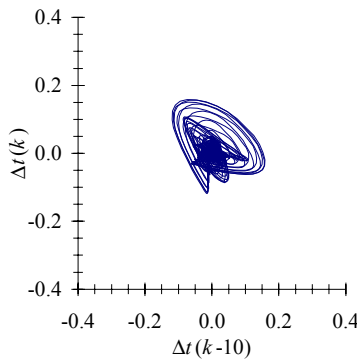


Fig. 18. 30% Dynamic Eccentricity Torque First Difference Phase-Space

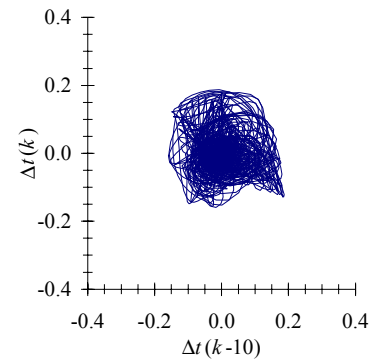


Fig. 19. One Broken Bar Torque First Difference Phase-Space

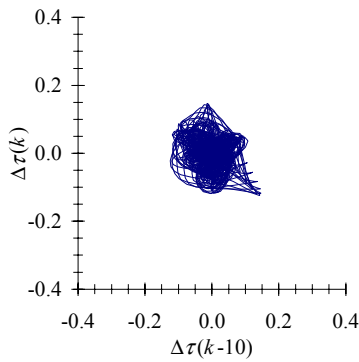


Fig. 20. Three Broken Bars Torque First Difference Phase-Space

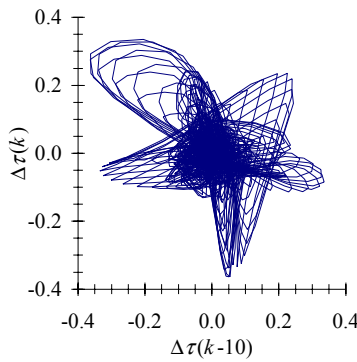


Fig. 21. Six Broken Bars Torque First Difference Phase-Space

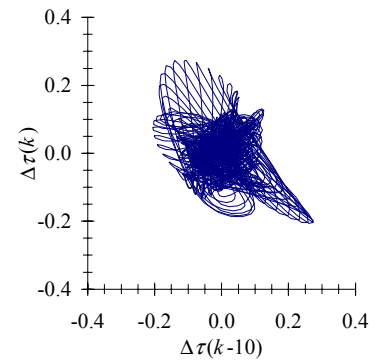


Fig. 22. Nine Broken Bars Torque First Difference Phase-Space

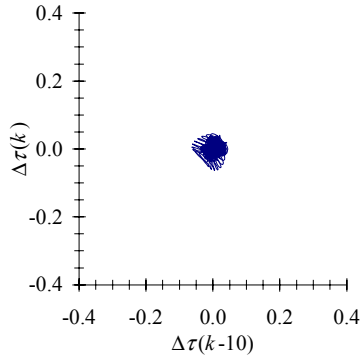


Fig. 23. Three Broken Connectors Torque First Difference Phase-Space

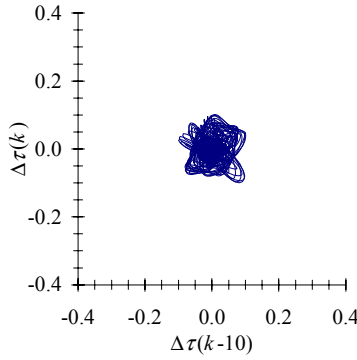


Fig. 24. Six Broken Connectors Torque First Difference Phase-Space

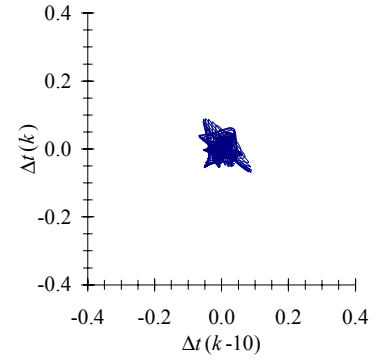


Fig. 25. Nine Broken Connectors Torque First Difference Phase-Space

V. RESULTS

From the TSCFE-SS model, we were able to obtain the time-domain simulations for longer time duration than the one cycle time series shown in Figs. 8 through 13 for the various torque profiles. Thus, one easily obtains an “out-of-sample” or “test” torque first difference time series for each of the 12 torque profile (torque first difference) cases analyzed by time delay embedding and radius of gyration calculations. Accordingly, the radius of gyration as a classifying feature was confirmed in the “out-of-sample” or “test” version of each motor mode of operation. The results are shown in Tables I and II for the sample simulations, and all compare well on a one to one correspondence with the out of sample values given in III and IV, for each case by case, respectively. For example, the sample or training radius of gyration for the healthy motor mode of operation is 0.0571, while the out-of-sample or testing radius of gyration is 0.0585. The sample and out-of-sample radii of gyration for the one broken bar motor mode of operation are 0.0892 and 0.0892, respectively. Likewise, the sample and out-of-sample radii of gyration for the 10% static eccentricity motor mode of operation are 0.0466 and 0.0469, respectively.

Operating Mode	Radius of Gyration
Healthy	0.0571
One Broken Bars	0.0892
Three Broken Bars	0.0635
Six Broken Bars	0.1100
Nine Broken Bars	0.0999
Three Broken Connectors	0.0247
Six Broken Connectors	0.0432
Nine Broken Connectors	0.0346
10 % Static Eccentricity	0.0466
30 % Static Eccentricity	0.0480
10 % Dynamic Eccentricity	0.0474
30 % Dynamic Eccentricity	0.0484

Operating Mode	Standard Deviation of the Radius of Gyration
10 % Static Eccentricity	0.0648
30 % Static Eccentricity	0.0662
10 % Dynamic Eccentricity	0.0654
30 % Dynamic Eccentricity	0.0663

Operating Mode	Radius of Gyration
Healthy	0.0585
One Broken Bars	0.0892
Three Broken Bars	0.0651
Six Broken Bars	0.1108
Nine Broken Bars	0.0994
Three Broken Connectors	0.0272
Six Broken Connectors	0.0441
Nine Broken Connectors	0.0348
10 % Static Eccentricity	0.0469
30 % Static Eccentricity	0.0483
10 % Dynamic Eccentricity	0.0473
30 % Dynamic Eccentricity	0.0487

Operating Mode	Standard Deviation of the Radius of Gyration
10 % Static Eccentricity	0.0648
30 % Static Eccentricity	0.0662
10 % Dynamic Eccentricity	0.0653
30 % Dynamic Eccentricity	0.0664

The results of the classification algorithm are shown in Tables V through VII. The headings for the tables are as follows: H – healthy motor, B1 – One Broken Bar, B3 – Three Broken Bars, B6 – Six Broken Bars, B9 – Nine Broken Bars, C3 – Three Broken Connectors, C6 – Six Broken Connectors, C9 – Nine Broken Connectors, S10 – 10% Static Eccentricity, S30 – 30% Static Eccentricity, D10 – 10% Dynamic Eccentricity, D30 – 30% Dynamic Eccentricity, respectively. The first column gives the actual mode of operation. The first row indicates the training radius of gyration that was used. The cells of Tables V and VI are the

[Training radius of gyration (given by the column heading) – Testing radius of gyration (given by the row heading)]. The minimal difference in each row, and thus the classification for all but the eccentricity motor modes of operation, is bolded. The cells of Table VII are the [Training standard deviation of the radius of gyration (given by the column heading) – Testing standard deviation of the radius of gyration (given by the row heading)]. The minimal difference in each row, and thus the classification, is bolded. The results illustrated in Tables V through VII confirm the validity of the approach, because of the small magnitudes of the absolute differences of these bolded radii of gyration and the absolute differences of these standard deviations of radii of gyration, in comparison to all the other differences in the tables (matrices).

TABLE V
ABSOLUTE DIFFERENCES BETWEEN TRAINING AND TESTING RADII OF GYRATION ($\times 10^{-2}$) PART I

	H	B1	B3	B6	B9	C3
H	0.143	3.069	0.503	5.151	4.136	3.384
B1	0.803	0.002	2.567	2.080	1.066	6.454
B3	5.368	2.409	0.156	4.491	3.477	4.043
B6	4.236	2.157	4.722	0.075	1.089	8.609
B9	2.987	1.025	3.590	1.057	0.043	7.477
C3	0.648	6.199	3.634	8.281	7.267	0.253
C6	2.226	3.859	1.294	5.941	4.927	2.593
C9	1.021	5.437	2.872	7.519	6.505	1.015
S10	0.879	4.232	1.667	6.314	5.300	2.220
S30	0.981	4.090	1.525	6.173	5.158	2.362
D10	0.840	4.193	1.628	6.275	5.261	2.259
D30	0.143	4.051	1.486	6.133	5.119	2.401

TABLE VI
ABSOLUTE DIFFERENCES BETWEEN TRAINING AND TESTING RADII OF GYRATION ($\times 10^{-2}$) PART II

	C6	C9	S10	S30	D10	D30
H	0.861	2.386	1.194	1.053	1.109	1.012
B1	3.932	5.457	4.265	4.124	4.180	4.083
B3	1.521	3.046	1.854	1.713	1.769	1.672
B6	6.086	7.612	6.420	6.279	6.335	6.238
B9	4.954	6.480	5.288	5.147	5.203	5.106
C3	2.269	0.744	1.936	2.077	2.021	2.118
C6	0.070	1.596	0.404	0.263	0.319	0.222
C9	1.508	0.018	1.174	1.315	1.259	1.356
S10	0.303	1.223	0.031	0.110	0.054	0.151
S30	0.161	1.365	0.173	0.031	0.087	0.009
D10	0.263	1.262	0.070	0.071	0.015	0.112
D30	0.122	1.404	0.212	0.071	0.127	0.030

TABLE VII
ABSOLUTE DIFFERENCES BETWEEN TRAINING AND TESTING STANDARD DEVIATION OF THE RADII OF GYRATION ($\times 10^{-2}$) PART II

	S10	S30	D10	D30
S10	0.003	0.140	0.057	0.155
S30	0.147	0.004	0.086	0.011
D10	0.052	0.091	0.008	0.106
D30	0.160	0.017	0.100	0.002

In other words, the classification accuracy on the out-of-sample or testing data is 100%. Beyond the classification accuracy, it is significant to point out that the classifications are robust in the sense that for most of the classifications the next nearest class has absolute difference of radii of gyration

that is one to two orders of magnitude greater than the correct class.

VI. LARGE SCALE IMPLEMENTATION

This proactive approach to fault diagnostics can head off the costly and catastrophic cascading of faults that lead to plant shutdowns and consequent long repair/maintenance periods. The resulting fault identification and diagnostic information also can facilitate the creation of efficient and effective maintenance schedules based on accurate classification of the nature and status of incipient faults associated with a particular motor drive. Hence, this technique has significant potential in applications to key induction motor ASDs such as in important process industries and similar applications where extended maintenance down times cannot be tolerated.

VII. CONCLUSIONS

In conclusion, this paper presents the integration of the TSCFE-SS method, which can generate a large number of faulty and healthy IMASD simulations, with the TSDM technique, which can automatically characterize and predict IMASD modes of operation. The method was shown to enable one to differentiate between types of faults such as dynamic and static eccentricities and distinguish them from squirrel-cage breakages. The method also distinguishes between the degrees of fault severities such as percentage eccentricities and number of bar as well as connector breakages. Once again, it should be reemphasized that the fault classification achieved by this methodology are robust, in the sense that for most of these fault classifications the next nearest class (other than the fault's calls) has absolute difference of radii of gyration that is one to two orders of magnitude greater than the correct (fault) class. Hence, this dual track approach can be used to head off the costly and catastrophic cascading of IMASD faults that lead to plant shutdowns and can facilitate the creation of efficient and effective maintenance schedules.

REFERENCES

- [1] M. E. H. Benbouzid, "Bibliography on Induction Motors Faults Detection and Diagnosis," *IEEE Transactions on Energy Conversion*, vol. 14, pp. 1065-1074, 1999.
- [2] J. F. Bangura and N. A. Demerdash, "Diagnosis and Characterization of Effects of Broken Rotor Bars and Connectors in Squirrel-Cage Induction Motors by a Time-Stepping Coupled Finite Element-State Space Modeling Approach," *IEEE Transactions on Energy Conversion*, vol. 14, pp. 1167-1175, 1999.
- [3] R. R. Schoen and T. G. Habetler, "Effects of time-varying loads on rotor fault detection in induction machines," *IEEE Transactions on Industry Applications*, vol. 31, pp. 900-906, 1995.
- [4] R. R. Schoen, B. K. Lin, T. G. Habetler, J. H. Schlag, and S. Farag, "Unsupervised, on-line system for induction motor fault detection using stator

- current monitoring,” *IEEE Transactions on Industry Applications*, vol. 31, pp. 1280-1286, 1995.
- [5] S. F. Farag, R. G. Bartheld, and T. G. Habetler, “Integrated on-line motor protection system,” *Industry Applications Magazine*, vol. 2, pp. 21-26, 1996.
- [6] F. Filippetti, G. Franceschini, and C. Tassoni, “Neural networks aided on-line diagnostics of induction motor rotor faults,” *IEEE Transactions on Industry Applications*, vol. 31, pp. 892-899, 1995.
- [7] J. F. Bangura and N. A. Demerdash, “Performance and Torque-Ripple Characterization in Induction Motor Adjustable Speed Drives Using Time-Stepping Coupled Finite Element State Space Techniques,” *IEEE Transactions on Industry Applications*, vol. 35, pp. 982-990, 1999.
- [8] N. A. O. Demerdash and J. F. Bangura, “Characterization of Induction Motors in Adjustable-Speed Drives Using a Time-Stepping Coupled Finite-Element State-Space Method Including Experimental Validation,” *IEEE Transactions on Industry Applications*, vol. 35, pp. 790-802, 1999.
- [9] J. F. Bangura and N. A. Demerdash, “Comparison Between Characterization and Diagnosis of Broken Bars/End-Ring Connectors and Airgap Eccentricities of Induction motors in ASDs Using a Coupled Finite Element-State Space Method,” *IEEE Transactions on Energy Conversion*, vol. 15, pp. 48-56, 2000.
- [10] J. F. Bangura and N. A. Demerdash, “Simulation of Inverter-Fed Induction Motor Drives with Pulse-Width Modulation by a Time-Stepping Coupled Finite Element-Flux Linkage-Based State Space Model,” *IEEE Transactions on Energy Conversion*, vol. 14, pp. 518-525, 1999.
- [11] R. J. Povinelli and X. Feng, “Temporal Pattern Identification of Time Series Data using Pattern Wavelets and Genetic Algorithms,” proceedings of Artificial Neural Networks in Engineering, St. Louis, Missouri, 1998, pp. 691-696.
- [12] R. J. Povinelli and X. Feng, “Data Mining of Multiple Nonstationary Time Series,” proceedings of Artificial Neural Networks in Engineering, St. Louis, Missouri, 1999, pp. 511-516.
- [13] R. J. Povinelli, J. F. Bangura, N. A. O. Demerdash, and R. H. Brown, “Diagnostics of Bar and End-Ring Connector Breakage Faults in Polyphase Induction Motors Through a Novel Dual Track of Time-Series Data Mining and Time-Stepping Coupled FE-State Space Modeling,” *IEEE Transactions on Energy Conversion*, in review.
- [14] J. F. Bangura and N. A. O. Demerdash, “Effects of Broken Bars/End-Ring Connectors and Airgap Eccentricities on Ohmic and Core Losses of Induction Motors in ASDs Using a Coupled Finite Element-State Space Method,” *IEEE Transactions on Energy Conversion*, vol. 15, pp. 40-47, 2000.
- [15] F. Takens, “Detecting strange attractors in turbulence,” proceedings of Dynamical Systems and Turbulence, Warwick, 1980, pp. 366-381.
- [16] H. D. I. Abarbanel, *Analysis of observed chaotic data*. New York: Springer, 1996.
- [17] P. A. Tipler, *Physics*, vol. 1, 2nd ed. New York, New York: Worth Publishers, 1982.